



# InSAR time-series investigation of long-term ground displacement at Beijing Capital International Airport, China



Mingliang Gao <sup>a,b,c,d</sup>, Huili Gong <sup>a,b,c,d,\*</sup>, Beibei Chen <sup>b,d</sup>, Chaofan Zhou <sup>c,d</sup>, Wenfeng Chen <sup>a,c,d</sup>, Yue Liang <sup>a,c,d</sup>, Min Shi <sup>c,d</sup>, Yuan Si <sup>c,d</sup>

<sup>a</sup> Base of the State Key Laboratory of Urban Environmental Process and Digital Modeling, Capital Normal University, Beijing 100048, China

<sup>b</sup> Key Laboratory of Resources Environment and GIS of Beijing Municipal, Capital Normal University, Beijing 100048, China

<sup>c</sup> Beijing Laboratory of Water Resources Security, Capital Normal University, Beijing 100048, China

<sup>d</sup> College of Resource Environment and Tourism, Capital Normal University, Beijing 100048, China

## ARTICLE INFO

### Article history:

Received 26 January 2016

Received in revised form 21 September 2016

Accepted 18 October 2016

Available online 20 October 2016

### Keywords:

InSAR

SBAS

Time-series

Land subsidence

Groundwater overdraft

## ABSTRACT

Interferometric synthetic aperture radar (InSAR) time-series analysis provides high spatial resolution and continuous temporal coverage for investigations of long-term ground displacement. Beijing, the capital city of China, has suffered from land subsidence since the 1950s, and extreme groundwater extraction has led to subsidence rates of >100 mm/year. In this study, InSAR time-series analysis is performed on different data subsets to investigate the ground displacement at Capital International Airport, Beijing, between June 2003 and November 2013. The results show that the ground surface in the airport has deformed at different rates ranging from -66.2 mm/year (sinking) to 8.2 mm/year (uplift) relative to the reference point. The projected vertical displacement rates agreed with measurements estimated from ground-leveling surveys, and the correlation coefficient of the fitting result is 0.96, with a standard deviation of 0.9 mm/year and a mean difference of 2.0 mm/year. The runways and terminals have been affected by land subsidence to various degrees. Previous studies has indicated that long-term intense groundwater extraction is the main reason leading to land subsidence in this area. Other triggering factors, such as active faults, the quaternary compressible layers and urbanization, also have different degrees of contribution or impact on land subsidence in Beijing Plain. Furthermore, some interesting behaviors from groundwater (such as inter- and semi-annual variations) and subsidence, the relationship between them are also found in this study.

© 2016 Elsevier B.V. All rights reserved.

## Index terms

1640

4315

4337

## 1. Introduction

Differential Interferometric synthetic aperture radar (D-InSAR) has been developed as a new geodetic technique over the past few decades. D-InSAR has been used for the measurement of topography and surface deformation (Stramondo et al., 2007), such as seismic deformation (Feng et al., 2014; Wang et al., 2014), volcanic-tectonic deformation (Ruch et al., 2009; Walter et al., 2015), glacial kinematics (Shugar et al., 2012; Neelmeijer et al., 2014), landslide (Calabro et al., 2010),

delta sinking (Higgins et al., 2014), and land subsidence (Stramondo et al., 2008; Calderhead et al., 2010; Ng et al., 2012; Liu et al., 2014).

Conventional D-InSAR can only extract the phase shifts between SAR image acquisition dates, rather than the time-series deformation rates, because of the short time span (Aobpaet et al., 2013). In addition, the application of conventional D-InSAR is mainly limited by temporal decorrelation, spatial decorrelation, and atmospheric delay, which are caused by different satellite observation positions, long image-acquisition intervals, and atmospheric fluctuations (Hanssen, 2001), respectively. All these issues can be addressed using time-series InSAR analysis methods, such as Small Baseline Subset (SBAS) (Berardino et al., 2002; Lanari et al., 2007) techniques. In the SBAS process, a network of interferogram pairs is created with a threshold for the temporal and spatial baseline criteria to limit decorrelation noise, unwrapping errors, and atmospheric delay errors (Yang et al., 2014). By forming interferograms from the images for a short time interval with small differences in the look and squint angle, decorrelation is minimized, and, at some resolutions, elements can be small enough, such that the underlying signal is still detectable (Hooper et al., 2012). Consequently, SBAS techniques have been widely used for detecting long-term and slow

\* Corresponding author at: College of Resource Environment and Tourism, Capital Normal University, Beijing 100048, China.

E-mail address: [gonghl\\_1956@126.com](mailto:gonghl_1956@126.com) (H. Gong).

deformation processes on the Earth's surface, such as land subsidence in metropolitan areas (Chaussard et al., 2014; Dong et al., 2014).

Land subsidence in metropolitan areas has been a common geological hazard for decades worldwide. >44,000 km<sup>2</sup> in 45 states in the USA and >70,000 km<sup>2</sup> in 17 provinces in China have suffered from land subsidence (Galloway et al., 1999; Hu et al., 2004; Xue et al., 2005). The spatial variety of land subsidence in urban areas often leads to damage to urban infrastructures including buildings, airports, railways, highways, subways, and other underground facilities. Several investigations based on InSAR technique have been implemented on urban infrastructures (Perissin et al., 2012; Lazecký et al., 2014; Short et al., 2014). Land subsidence in urban areas is mainly caused by human activities, including over-exploitation of groundwater (Calderhead et al., 2010) or oil/gas (Gambolati et al., 2001; Ferronato et al., 2008), underground works, and massive construction of high buildings (Jie et al., 2007). Measurements of land subsidence in Beijing, the capital city of China, show that the total subsidence is >1100 mm, with a maximum sinking velocity of 137.5 mm/year in some regions by the end of 2009 (Liu et al., 2012b). A previous study showed that the land subsidence in Beijing was comprehensively affected by over-exploitation of groundwater (Hu et al., 2014), urban construction (Chen et al., 2015b), and geological fault structures and that the mechanisms of land subsidence are complex in different areas (Chen et al., 2015a).

In this study, we use 47 Envisat ASAR images (from 2003 to 2010) and 33 TerraSAR-X images (from 2010 to 2013) that cover the Beijing Plain and the northern part of the plain, respectively. The Stanford Method for Persistent Scatter/Multi-Temporal Interferometry (StaMPS/MTI) SBAS technique (Hooper, 2008) was used to obtain the time-series land displacement information for Capital International Airport in north Beijing. The distribution of surface deformation over the whole coverage of the data stacks is also obtained. The study site is described in Section 2, and the SBAS technique is presented in Section 3, followed by details of the data processing. Results, validation and discussion are provided in Sections 4 to 6, respectively. The main conclusions of this study are presented in the final section.

## 2. Study site and data description

### 2.1. Study site

Beijing, the capital city of China, is located in the north of the North China Plain and occupies the region between 39.4°N, 115.7°E and 41.6°N, 117.4°E, with a total area of 16,410.54 km<sup>2</sup>. As illustrated in Fig. 1, the city itself lies on the Beijing Plain (with an average elevation of 43.5 m), which opens to the east and south and surrounded by mountains (with the highest elevation of 2303 m) from the southwest to the northeast. The Beijing Plain is a typical piedmont alluvial diluvial plain formed from sediment carried by the Yongding, Chaobai, and Wenyu rivers. The Quaternary sediments from the piedmont to the plain areas are generally divided into three parts: alluvial-pluvial fan in the top, alluvial-pluvial fan in the middle, and fringe part of alluvial-pluvial fan and alluvial plain area (Liu et al., 2012a). The climate is temperate semi-humid continental monsoon type: the annual average temperature is approximately 10 °C–12 °C, and the mean annual precipitation is 510 mm.

The airport is located in the northeast of downtown Beijing in Shunyi County. The airport lies in the flat area (elevation 22.0–35.4 m) between the Wenyu River and Chaobai River alluvial–proluvial fans, at the end of the Yongding River alluvial–proluvial fan. The airport was built in 1958, and was the first civil airport in PR China. As shown in Fig. 1, there are three terminals (T1, T2, and T3) and three runways in the airport. The runways are numbered 36 L, 36R, and 01 and have lengths of 3200, 3800, and 3800 m, respectively. Terminal T3 and runway 01 were built in 2008 to cope with the extra Olympic visitors; construction began in March 2004. In 2014, the airport handled a total of 581,953 air traffic movements, 86,128,270 passengers (the second highest in the world), and 1,848,251 tons of cargo, representing year-on-year decreases of 2.5%, 2.9%, and 0.2%, respectively.

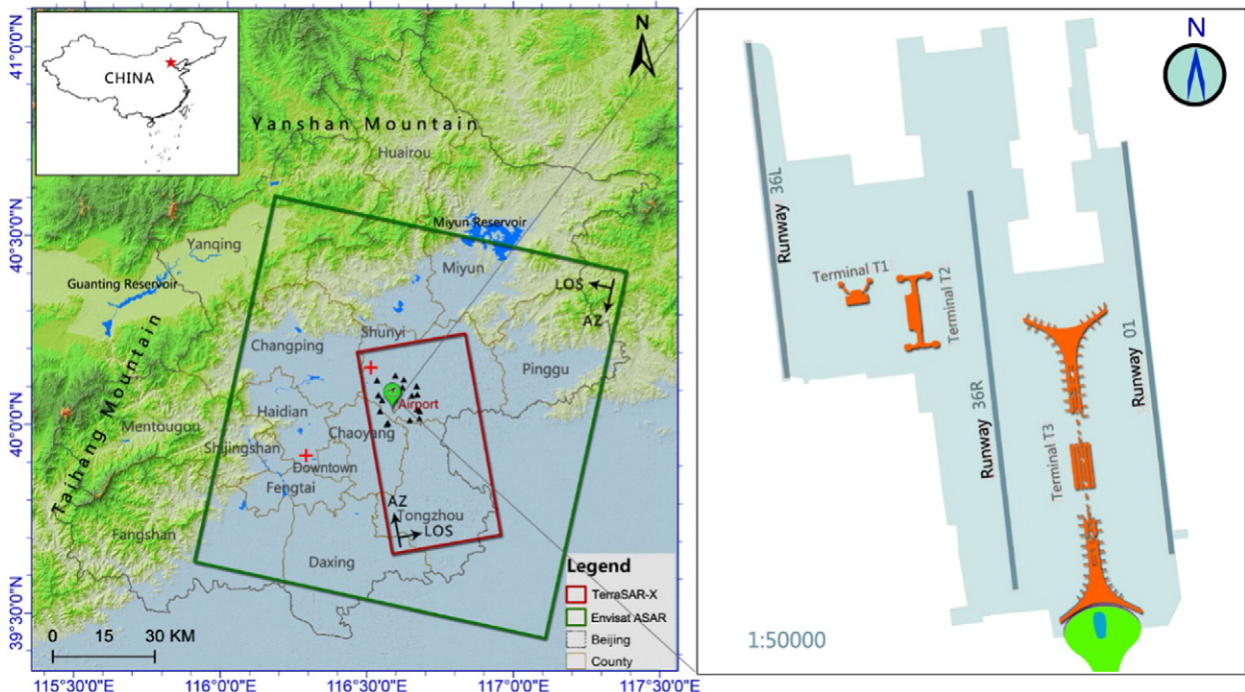


**Fig. 1.** The location of the study site and a sketch map of the airport. The red star indicates the location of Beijing. The boxes represent the frames of the used SAR data. The red cross indicate the geographical locations of the reference points used in the two tracks of InSAR measurements. The black triangles indicate the geographical locations of the benchmarks of the ground leveling survey. AZ and LOS represent the azimuth and line-of-sight (LOS) directions respectively.

## 2.2. Data description

The dataset used in this study consists of a stack of Envisat ASAR images and two stacks of TerraSAR-X images, covering areas of approximately 10,000 km<sup>2</sup> and 1500 km<sup>2</sup>, respectively. The stack of 47 ASAR images acquired from Jun. 2003 to Aug. 2010 from the descending track was provided by the European Space Agency. The maximum temporal baseline is 1960 days, and the perpendicular baseline ranges from 39.8 to 1011.8 m (Fig. 2a). Two time-series TerraSAR-X & TanDEM-X (TerraSAR-X add-on for Digital Elevation Measurement) datasets acquired from ascending track at different bandwidths were provided by the German Aerospace Center (German: Deutsches Zentrum für Luft- und Raumfahrt e.V., abbreviated DLR). One stack of 18 images recorded at 100 MHz was acquired from Apr. 2010 and Dec. 2011, with a maximum temporal baseline of 396 days and a perpendicular baseline between 12.4 and 453.3 m. The other stack of 15 images recorded at 150 MHz was acquired from Jan. 2012 to Nov. 2013, with a maximum temporal baseline of 396 days and the perpendicular baseline ranging from 0.6 to 368.0 m (Fig. 2a). Both the stacks were single-polarization HH mode images recorded in stripmap mode with a resolution of up to 3 m.

It is important to note that TanDEM-X is the name of TerraSAR-X's twin satellite, and it is a second, almost identical spacecraft to TerraSAR-X. The TanDEM-X mission is designed to generate a global

digital elevation model (DEM) with 12-m resolution and a vertical accuracy better than 2 m (Krieger et al., 2007).

## 3. Methods and data processing

We conducted the time-series DInSAR survey of the airport area from the three data stacks using the SBAS toolkit provided by StaMPS/MTI (available at <http://homepages.see.leeds.ac.uk/~earahoo/stamps/>). During the SBAS procedure, pixels that remain coherent within the interferogram pairs are identified. Consequently, it is possible to identify and measure millimeter-scale displacements in the satellite's LOS direction.

The main procedure of the SBAS technique is illustrated in Fig. 2b: other processes such as image cropping, multi-looking, resampling, and image filters are not included. The preprocessing steps should be already performed before SBAS: master selection, co-registration, orbit calculation, and terrain removal. Generally, the first step of the SBAS technique is the generation of differential interferograms between small baseline SAR data pairs (Tizzani et al., 2007). These interferograms are formed base on the single-master interferograms generated by Doris (Delft object-oriented radar interferometric software, <http://doris.tudelft.nl>), an open source InSAR processor. To generate the SAR pairs, individual connections can be adjusted by editing the small-baselines.list file, which is created by StaMPS (Hooper et al., 2013,

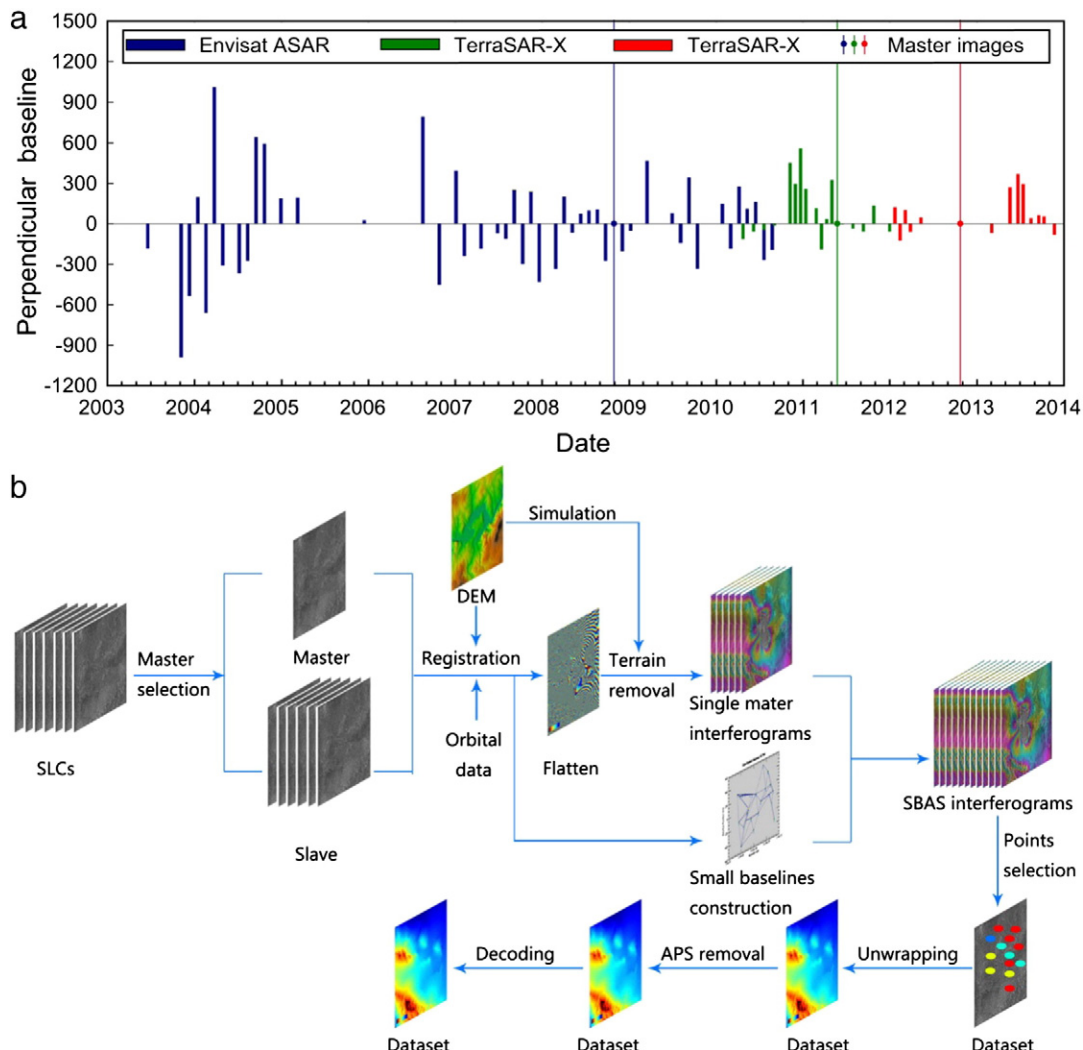


**Fig. 2.** (a) Temporal-spatial baseline distributions of Envisat ASAR and TerraSAR-X image stacks. (b) The sketch up of StaMPS SBAS technique. The StaMPS SBAS processing is based on the single master interferogram pairs created by Doris.

p.22). For StaMPs SBAS procedure, there should be no isolated clusters of images; otherwise, the process will be discontinued during phase unwrapping.

After the SBAS interferograms are created, there will be an iterative step that estimates the phase noise value for each candidate pixel in every interferogram. Noise can be further reduced using spatial filters; however, spatial filters in the range and azimuth direction reduce the spatial resolution, which probably causes failure to identify some high coherent points. In many small baseline algorithms, the interferograms are then multilooked to further decrease decorrelation noise (e.g., Berardino et al., 2002; Schmidt and Bürgmann, 2003). However, there may be isolated coherent resolution ground elements that are surrounded by incoherent elements, for which multilooking will increase decorrelation. Therefore, the SBAS process is implemented at full resolution (Hooper, 2008). For pixels whose phase decorrelates little over short time intervals, which Hooper (2008) refers to as slowly-decorrelating filtered phase (SDFP) pixels, are the targets of SB methods. Pixels are selected based on phase analysis and estimated spatial coherence. Then the phase is unwrapped using a statistical cost flow algorithm named “3-D” approach (Hooper, 2009). The spatial-correlated look angle (SCLA) error and atmosphere and orbit error (AOE) phase are estimated after phase unwrapping. Separation of atmospheric effects is achieved by filtering the time series in time and space domain.

In this study, we use the ASTER Global Digital Elevation Model Version 2 (ASTER GDEM V2) with 30-m resolution as extra DEM for registration, terrain phase simulation, and terrain removal. The ASTER GDEM is repaired by SRTM DEM through least square method before registration, since there are negative values in some flat areas. On the basis of our data set, we set the thresholds including minimum coherence, maximum temporal difference, and maximum perpendicular baseline difference as 0.5, 300 days, and 500 m, respectively.

The vertical displacement is considered to be more appropriate for the flat airport area and is necessary for comparison with ground leveling measurements. For SAR side-looking geometry, the detected velocity along the LOS direction is the geometrical sum of three-dimensional deformation projected to the LOS direction, as shown in Eq. (1):

$$d_{\text{los}} = -\sin\theta \sin(\alpha - 3\pi/2) \cdot d_x - \sin\theta \cos(\alpha - 3\pi/2) \cdot d_y + \cos\theta \cdot d_z \quad (1)$$

where  $d_x$ ,  $d_y$ , and  $d_z$  are the velocities in west–east, south–north and vertical direction, respectively.  $\alpha$  is the heading angle and  $\theta$  is the incidence angle. In our case, for ascending track (TXS),  $\alpha$  is 349.8° and  $\theta$  is 35.2°, while for descending tracks (ASAR),  $\alpha$  is −164.3° and  $\theta$  is 22.9°. Then, Eq. (1) can be written as follows:

$$\begin{aligned} d_{\text{los,asc}} &= -0.57d_x - 0.10d_y + 0.82d_z \\ d_{\text{los,desc}} &= 0.38d_x + 0.11d_y + 0.92d_z \end{aligned} \quad (2)$$

In Eq. (2), the system has a very low sensitivity to the S-N component. Owing to the polar orbit of the SAR satellites, the S-N component of the deformation is negligible (Luo et al., 2014) and the nature of the investigated signal is dominantly vertical (Marie and Manoochehr, 2015). The assumption is also supported by previous works, in which GPS (Xie et al., 2002) and leveling (Guo et al., 2003) investigations show that this area presents a low relative horizontal movement (1.57–1.93 mm/year). Thus, the SBAS-measured displacements were directly projected into the vertical direction, assuming that the detected movements are mostly in vertical direction during the period spanned by SAR image acquisition in this study.

The SBAS-measured displacement map was generated by inverse distance weighted (IDW) interpolation, with a resolution consistent with the ASAR image (geometrical resolution of 30 m). To obtain the time-series measurement and cumulative displacement of the entire time interval spanned by the three individual stacks, cubic spline interpolation was performed on the SBAS-measured displacement in the time domain. Fortunately, there were two images with the same

acquisition date (July 21, 2010) in the Envisat ASAR stack and the TerraSAR-X stack. Thus, the measurements from the TerraSAR-X stack (acquired between April 2010 and December 2011) were recalculated with respect to the reference benchmark. Similarly, the displacement measured from the other TerraSAR-X stack (acquired between January 2012 and November 2013) was also recalculated by cubic spline interpolation with respect to the reference point.

## 4. Results

As mentioned above, the construction of the airport extension project started in 2004, and it included terminal T3 and the new 4F runway (Runway 01), warehouses, and other supporting facilities. We divided the results obtained from the ASAR stack into three subsets on the basis of the extension project schedule. Therefore, a total of five time-series displacement rates were obtained, including the results derived from the two TerraSAR-X stacks, as displayed in Fig. 3. Negative values indicate downward movement in the vertical direction; positive values indicate uplift in the vertical direction. The displacements obtained from the ASAR stack (Fig. 3a–3c) are given relative to a reference point, which is marked with a red cross in Fig. 1. The displacements of the two TerraSAR-X stacks (Fig. 3d–3e) are given relative to a measurable point (a corner reflector marked as a cross in Fig. 1a) because of the lack of reference points. In this case, the chosen point will have been equally affected by the measurement as well as the displacement rates obtained from the TerraSAR-X stacks.

The displacement rate map generated from the SAR stacks is shown in Fig. 3. The results showed that the land in the airport has deformed at different rates, between −66.2 mm/year (sinking) and +8.2 mm/year (uplift) relative to the reference points, between June 2003 and November 2013. Initially, there are more pixels detected in the TerraSAR-X stacks (2735 points) than in the ASAR stack (1812 points), particularly in the reconstruction area. On one hand, the TerraSAR-X image has higher ground resolution in both range and azimuth than the ASAR image; on the other hand, the land cover of the extension project area varied with time, and in this case, few SDFP pixels can be detected.

Fig. 3b shows the lowest deformation rate (mm/year) during the terminal T3 construction from Apr. 2004–Feb. 2008, compared to other panels in Fig. 3. As can be seen from Table 1 and Fig. 5, most of the subsidence rates (absolute value) from InSAR observation and leveling time series during this period are simultaneously smaller than these in other time spans. The mitigation of subsidence rate mainly benefits from the limitation of groundwater exploitation forced by the government. And then the groundwater level slow its falling speed (Fig. 7d). Nevertheless, when examined the historical satellite images, we found that the land cover in this area (red triangle in Fig. 3b) has greatly changed from 2004 to 2008. Unfortunately, the sparse SAR acquisitions (two for 2005 and 2006, four for 2007) during the short construction period of the new subsidiary facilities (such as warehouse) makes it amphibolous to identify SDFP pixels. In this case, the detected SDFP pixels are derived from different source (in other words, from time-varying objects), such as bungalows in the beginning, then building materials, mobile houses, and finally the designed facilities. This measurement of variations resulted in strong non-linear deformations but escaped from the filtering after phase unwrapping. Thus, we consider the measurements cannot reflect the real deformation of the surface in this area in this period.

In Fig. 4, the displacements in the airport area are spatially uneven, with subsidence rates increasing from southeast to northwest. It is clear that the time-series deformation rates of the airport area were gradually reduced because more blue points appeared through time. However, the terminals T1 and T2 suffered from minute but relatively homogeneous settlement deformation with rates of about −40 mm/year. In addition, a sinking area (red areas) with a deformation rate under −50 mm/year has gradually formed in the cargo section (in the north of the airport area) during the measurement period. The red-

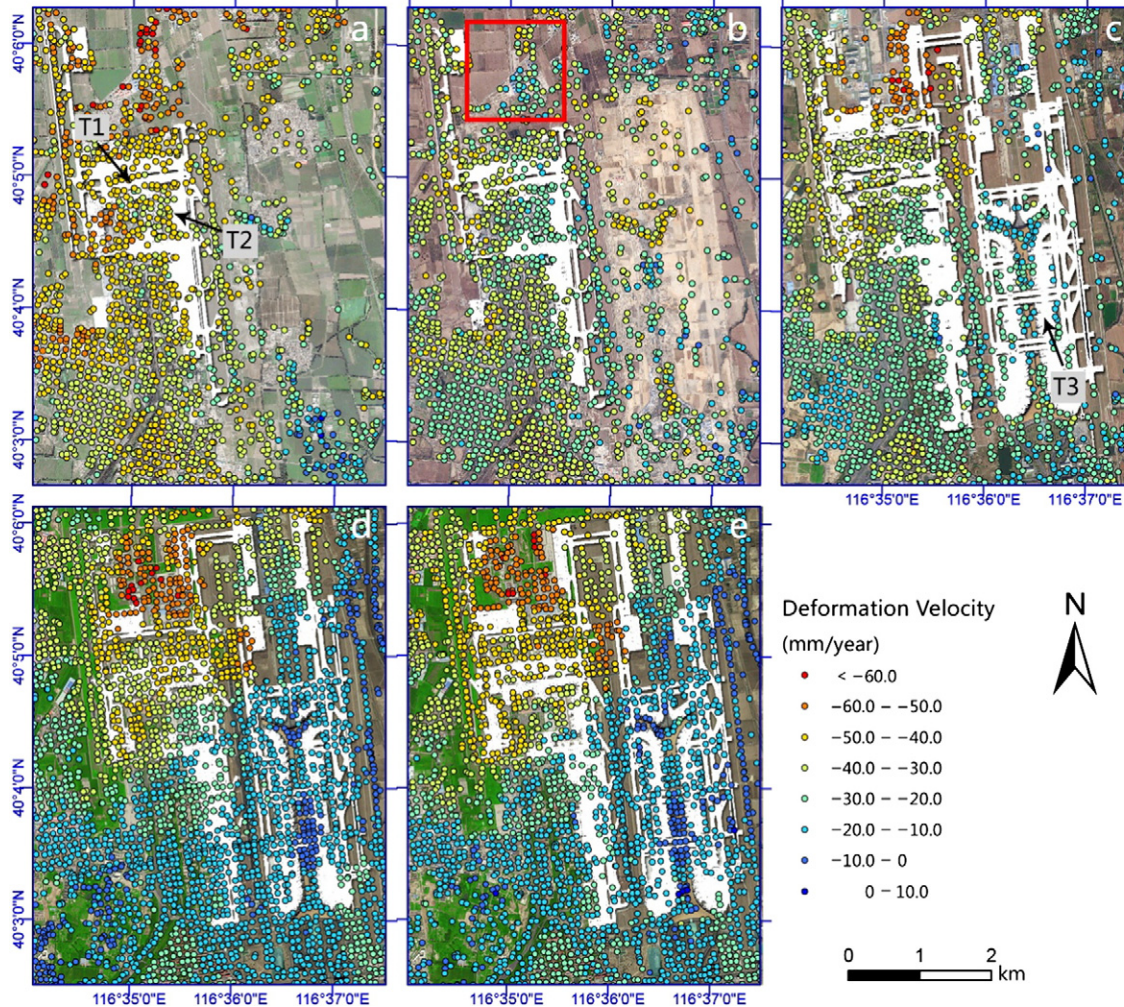


**Fig. 3.** Ground displacement rate (mm/year), (a) before T3 construction (2003.6–2004.3), (b) during T3 construction (2004.4–2008.2), (c) after T3 construction (2008.4–2010.8), and (d) 2010.9–2011.12. (e) 2012.1–2013.11. (a)–(c) were obtained from the Envisat ASAR stack; (d) and (e) were derived from the two TerraSAR stacks.

orange area (marked with a red circle in Fig. 4e) is more clearly visible in the IDW interpolated map. Furthermore, it is worth noting that there is a smaller subsidence bowl (black circle in Fig. 4e) forming north of the runway 36R, which may be affected by subsidence deformation.

## 5. Comparison with ground leveling measurements

To evaluate the accuracy of the SBAS measurements, it is necessary to compare the time-series results with displacement values acquired

**Table 1**

Comparison of mean subsidence rates (mm/year) between SBAS time-series and leveling at the 15 benchmarks. The larger differences between SBAS and leveling are in bold type.

Benchmark identifier	2005.9–2008.9 (mm/year)			2008.9–2010.9 (mm/year)			2010.9–2013.9 (mm/year)		
	SBAS	Leveling	Diff.	SBAS	Leveling	Diff.	SBAS	Leveling	Diff.
BJ006	−34.4	−37.0	2.6	−43.6	−41.9	−1.7	−41.9	−42.6	0.7
BJ007	−15.1	−12.9	−2.2	−20.4	−19.3	−1.1	−19.9	−18.4	−1.5
BJ018	−40.4	−37.9	−2.5	−43.6	−46.1	2.5	−45.1	−44.0	−1.1
BJ046	−29.7	−26.9	−2.8	−45.6	−43.0	−2.6	−43.5	−44.5	1.0
BJ050	−23.5	−26.0	2.5	−24.6	−22.7	−1.9	−28.0	−29.0	1.0
BJ061	−13.5	−15.9	2.4	−18.1	−16.9	−1.2	−16.3	−15.0	−1.3
BJ066	−30.9	−28.3	−2.6	−30.5	−28.5	−2.0	−29.7	−32.4	2.7
BJ102	−29.9	−32.1	2.2	−36.7	−34.8	−1.9	−26.7	−27.4	0.7
BJ156	−19.7	−22.2	2.5	−31.3	−29.6	−1.7	−25.3	−26.8	1.5
BJ157	−41.1	−41.5	0.4	−37.5	−36.0	−1.5	−49.5	−47.2	−2.3
BJ158	−25.4	−22.8	−2.6	−39.4	−36.3	−3.1	−36.5	−34.1	−2.4
BJ161	−15.8	−17.9	2.1	−29.4	−27.3	−2.1	−26.0	−24.3	−1.7
BJ162	−16.1	−16.6	0.5	−26.5	−23.8	−2.7	−25.2	−25.3	0.1
BJ163	−13.7	−15.8	2.1	−21.4	−20.5	−1.9	−23.2	−26.0	2.7
BJ164	−26.3	19.0	<b>−7.3</b>	−33.4	−25.5	<b>−7.9</b>	−40.7	−33.5	<b>−7.2</b>

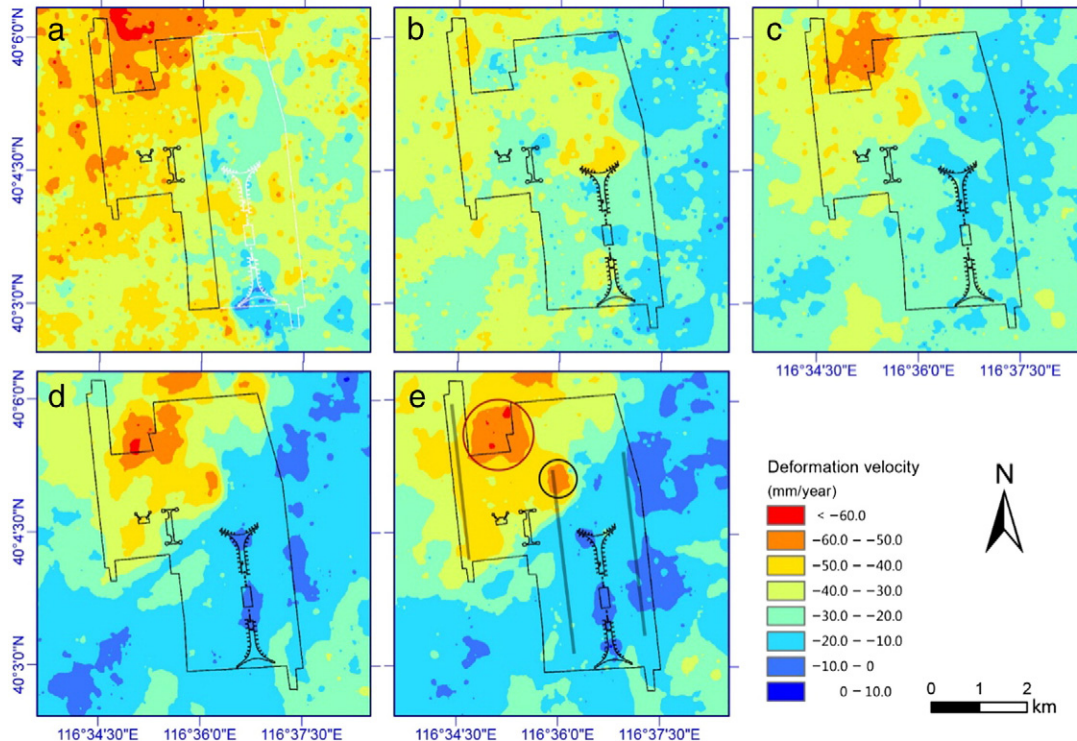


**Fig. 4.** IDW interpolation results of Beijing Capital Airport from InSAR time-series analysis, corresponding to the time table in Fig. 3.

using other techniques (Raucoules et al., 2003). In this study, ground leveling survey data acquired annually from September 2005 to September 2013 were obtained for validation of the InSAR time-series measurements. Leveling survey data from 15 benchmarks (indicated by black triangles in Fig. 1) near the airport were used in this study. The average displacement of pixels lying at a distance of <100 m from each benchmark was obtained using the corresponding InSAR measurement with the assumption that the surface does not change significantly over this distance.

Comparison between InSAR-measured and leveling-measured displacement time-series was performed by recalculating the leveling time-series displacement with respect to the reference benchmark and the initial time (September 15, 2005) of ground leveling measurements. To compare the displacement time-series obtained from both measurements, cubic spline interpolation was performed on the SBAS-measured displacement in the time domain.

### 5.1. Mean displacement rate

Interpolation in the time domain was also used for quantitative comparison of the cumulative displacement time-series measured from both techniques. The SBAS-measured displacements were interpolated to the dates of the ground leveling surveys. We compare the mean subsidence rate from SBAS time-series measurement and ground leveling using the reference point marked in Fig. 1 as a reference. Table 1 shows the 3 different mean rates at the 15 benchmarks estimated from both techniques.

It can be seen from Table 1 that most of the mean rates from leveling at every benchmark agree with the InSAR based measurement. Most of the differences between the two measurements vary from 0.1 mm/year to 3.1 mm/year. Nevertheless, we find that for benchmark BJ164, there are significant differences (>7 mm/year) between leveling and SBAS time-series rates. We are sure that selection of the reference point

cannot be the cause of the differences between leveling and InSAR because otherwise all the time series would be affected. It seems that the natural scatterers on the ground nearby are moving down about 7.5 mm/year faster than the benchmark. Unfortunately, after investigating we find there is an area with significant unwrapping errors due to sparse coherent points near the BJ164 benchmark. Through the field investigation we find that most of the InSAR signals are relate to buildings and scattered infrastructures, and in this case, most of the measurements from InSAR agree with the leveling benchmark. In this case, we remove the No. BJ164 benchmark and plot the mean subsidence rates from interpolated InSAR time-series analysis and ground leveling at the 14 benchmarks onto a scatter chart, then statistical results are obtained through least square fitting. The differences between the two measurements vary from -0.1 mm/year to 3.1 mm/year with a mean difference of 2.0 mm/year, the standard deviation (SD) is 0.9 mm/year, and the correlation coefficient ( $r^2$ ) is 0.96.

### 5.2. Time-series

We plot the time series of land subsidence from InSAR and ground leveling measurements to inspect the developing trend of the subsidence in time domain. Fig. 5 shows the locations of the benchmarks are persistently sinking and the time-series measurements from both techniques agreement reasonably well; however, the temporal sampling rate of the leveling surveys (annual) is much lower than that of the SAR acquisitions (almost monthly). Although the measured displacements between the two techniques are in general agreement, there are strong non-linear deformations detected by InSAR time-series analysis since 2004, which are not obvious in ground leveling surveying due to the poor temporal sampling. Besides, as mentioned in Section 4, the faults occurred in identifying SDFP pixels could result in strong non-linear deformations. In this case, when plot the InSAR measured subsidence time series for the benchmarks, we note that the scatterplots in

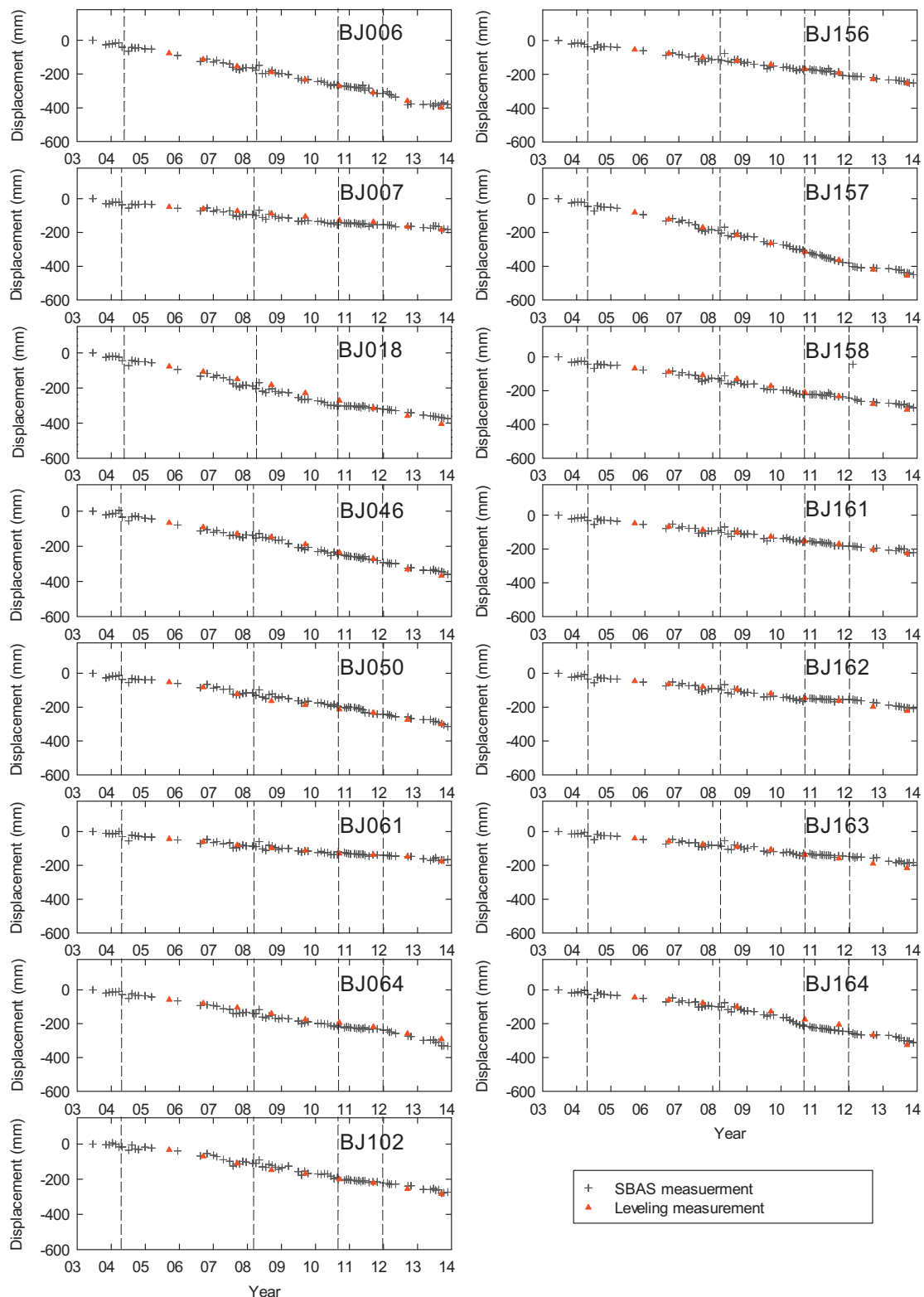


**Fig. 5.** Comparison between the vertical displacements measured by SBAS time-series analysis and by ground leveling surveys at fifteen benchmarks during the span of SAR acquisitions.

**Fig. 5** exhibit fluctuations during 2004–2005 and 2007–2008 (**Fig. 5**). Nevertheless, we note that atmospheric delay also contributes to the noise for the InSAR time-series, and actually it is difficult to separate it from no-linear deformation. As a consequence, it turn to be more complex to assess the non-linear deformation and is beyond the scope of this article, since the SBAS cannot separate the non-linear component from the linear component.

## 6. Discussion

### 6.1. Combination of Envisat ASAR and TerraSAR-X SBAS measurements

In this study, three SAR acquisition stacks from different observation platforms were used in the SBAS measurements. In this case, both IDW interpolation and cubic spline interpolation were used in the calculation

of the cumulative displacements. IDW interpolation in the space domain was performed to obtain the surface displacement in order to allow for differences between pixels extracted from different stacks. In addition, cubic spline interpolation in the time domain was used to estimate the displacements on the date without SAR acquisition. Although the pixels from different sensors were directly interpolated for calculation without datum transformation, comparison with the leveling measurements has demonstrated the reliability of the interpolated time-series results.

## 6.2. Cumulative displacements of the runways

As shown in the SBAS-interpolated displacement rate map (Fig. 4), the runways at the airport in Beijing have been sinking to varying degrees over the past few years. Thus, SBAS-interpolated cumulative displacement maps were generated through IDW interpolation and cubic spline interpolation on discrete pixels in the space and time domains, respectively. The runway pixels extracted from the interpolation results are shown in Fig. 6(a). The measurements suggest that cumulative displacement occurred for all the pixels over the 5-year (runway 01) or 10-year (runways 36L and 36R) periods spanned by the SAR data.

The average cumulative displacements observed are  $-399.6$ ,  $-286.0$ , and  $-104.8$  mm on runways 36 L, 36R, and 01, respectively. The maximum cumulative subsidence observed is 464.7 mm, at the pixel located on north of runway 36R. The profile map in Fig. 6b clearly shows the surface fluctuations of the runways. Runways 36L and 01 have sunk relatively evenly by approximately 400 mm and 105 mm during the SAR acquisitions, respectively. In contrast, runway 36R dropped  $>200$  mm in the north relative to the sinking surface (approximately  $-200$  mm) within a horizontal distance of 1000 m, which is under the runway construction standards ( $\pm 1\%$ ). It can be concluded that the three runways in the airport have experienced subsidence to differing degrees, although the deformations are within allowable limits.

## 6.3. Relationship between land subsidence and groundwater level

In Beijing, subsidence is taking place at average rates of 10–20 mm/year over a large area, while rapid-subsidence bowls (rates  $>100$  mm/year) are forming in Chaoyang (south of the airport area) and Tongzhou (red area in Fig. 7a). A previous study showed that the subsidence in Beijing is mainly caused by intense groundwater extraction, apart from the hydrogeological conditions; however, the uneven distribution of the land subsidence has been strongly affected by the presence of compressible deposits (Zhu et al., 2015). In Beijing, deep water has been extracted at high rates for industrial and agricultural uses. However, the reported groundwater extraction volumes cannot be used because of the large number of unregistered wells. Thus, we compared the mean subsidence rate between Jun. 2003 and Aug. 2010 and the average groundwater table between 2003 and 2010. As illustrated in Fig. 7a, the distribution of subsidence matches that of the low-lying groundwater table, and areas with high subsidence rates are always located in areas with a low groundwater table (such as groundwater depression cone). Nevertheless, the spatial distributions of the subsidence rate and the groundwater depression cones are not fully aligned with each other.

For detailed analysis about the correlation between land subsidence and groundwater pumping, we plot the monitoring results of the confined groundwater superimposed by interpolated InSAR time-series measurements from the four wells (marked in red in Fig. 7a). Well No. 50002 is located near the center of the Tianzhu-tongzhou funnel while well No.30010 is located at the edge of the funnel. Another two wells are located in western area. For the locations of the well No. 30010 No. 40016, and No. 50002, the measured subsidence increases along with the underground water level. Although the measurements cannot keep very strict relationship, they point toward the same trend and can be good verifications to the conclusion from Prof. Zhu et al. in 2015.

The poroelastic response to groundwater withdraw is detected as surface deformation due to elastic recoverable subsidence or inelastic,

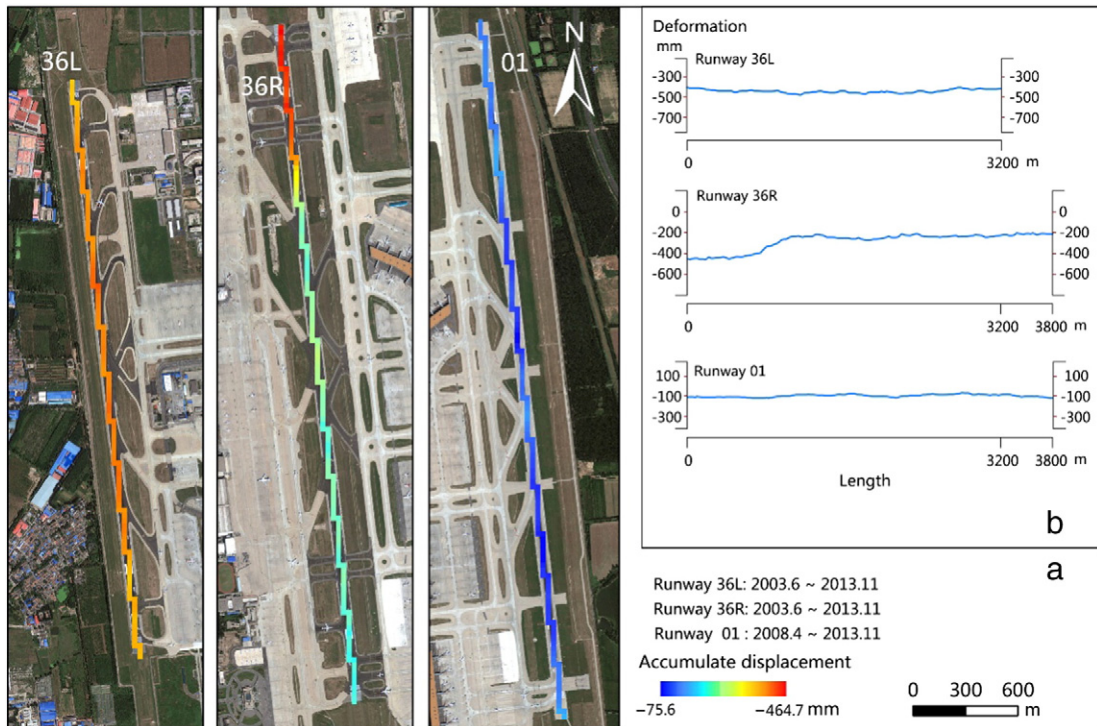


**Fig. 6.** Cumulative displacement map of the three runways extracted from the inverse distance-weighted interpolation results obtained from InSAR time-series analysis (a), and profiles of the three runways from the cumulative displacement results of InSAR time-series analysis (b).

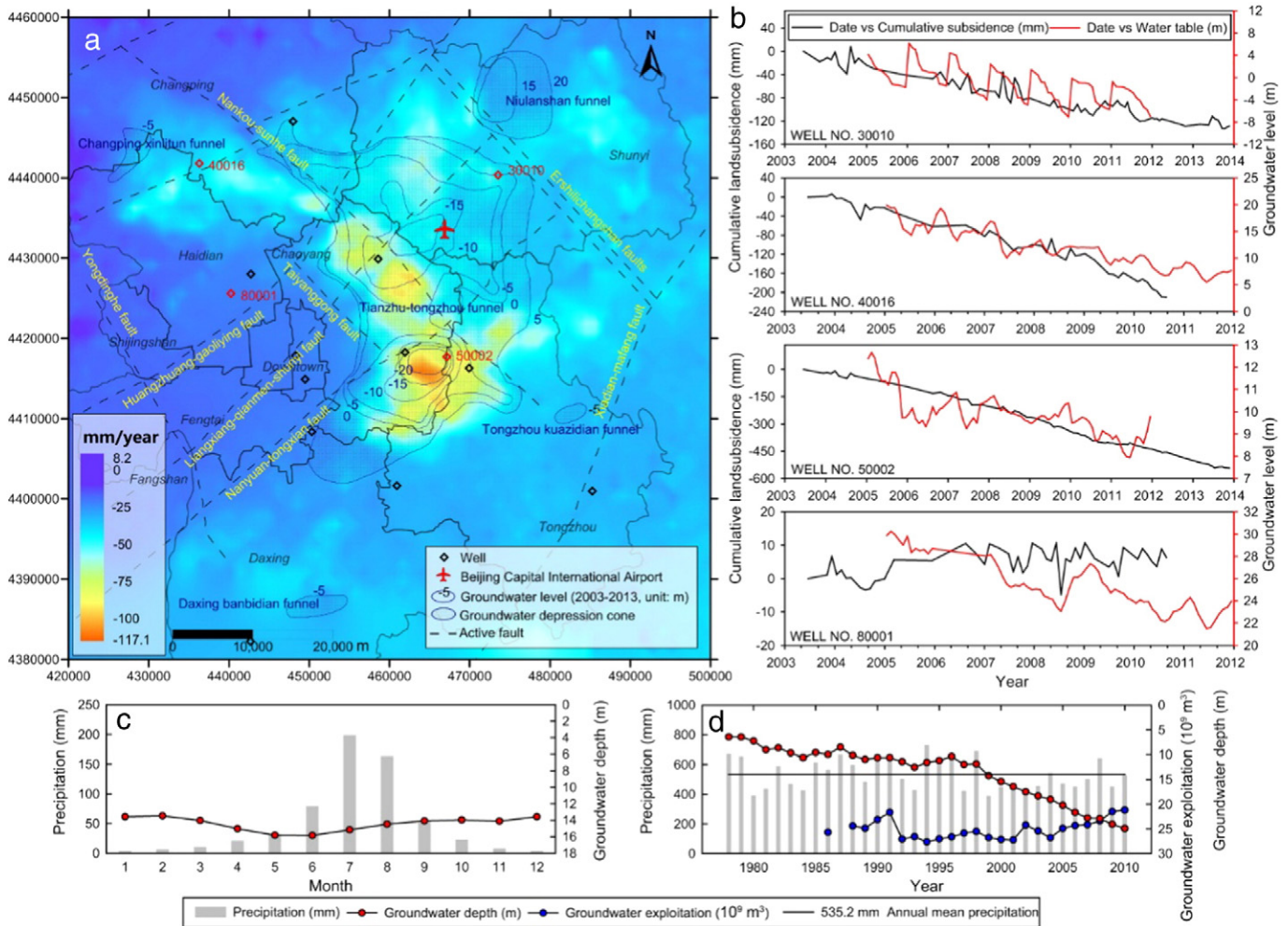


**Fig. 7.** (a) Overlap of main active faults and SBAS-measured mean subsidence rate between Jun. 2003 and Aug. 2010 with the average groundwater table contours for the same period. The diamonds stand for wells for the exploitation of groundwater around the land subsidence area. (b) Comparison of well-logging groundwater level and InSAR time-series measured displacement between 2003 and 2013. (c) Monthly mean precipitation vs. monthly mean groundwater depth from 1978 to 2010 in Beijing Plain. (d) Annual precipitation vs. annual mean groundwater depth vs. annual mean groundwater exploitation from 1978 to 2010.

permanent compaction (Marie and Manoochehr, 2015). Well No. 80001 present elastic behaviors as when the groundwater is missing (i.e., water level falls caused by pumping), pore pressure is reduced and the surface sinks. Conversely, when the pore pressure is regained by natural or artificial recharge (i.e., due to water level recovery), elastic relaxation of the aquifer systems occurs, which in turn leads to soil expansion (i.e., surface uplift) (Galloway et al., 1999). While well No. 50002 shows an obviously inelastic, permanent subsidence as the aquifer system presents a continuous compaction associated with the groundwater level decrease (Fig. 7b).

Since the Wheat-Maize double cropping system plays a very important role in agriculture production in North China Plain, irrigation of winter wheat in Beijing Plain is implemented according to the solar term. As shown in Fig. 7c, little rainfall but a large amount of water for agricultural demand between Mar. and Jun. lead to the rapid drop of water level; then groundwater rise between Jul. and Sep. benefitting from plentiful rain and less agricultural consuming. However, in general, the decline of groundwater prevails. Even after 2004, as can be seen in Fig. 7d, groundwater depth in Beijing Plain was increasing year by year despite the decrease of the groundwater exploitation. On one hand, the lack of rain makes it difficult to form effective groundwater recharge; on the other hand, the groundwater system in Beijing Plain has been partly damaged by long time overexploitation of groundwater.

In this case, the water level at well No. 30010 located near farmland presents a strong seasonal characteristics, because a large amount of groundwater is seasonally pumped for agriculture irrigation in this area. Nevertheless, it seems that the time-series subsidence here is not strongly affected by the seasonal change of the groundwater.

After continuous wavelet transform (CWT) analysis on the time series of ground water level and InSAR measurements at well No. 30010, we plot the wavelet variance and the CWT coefficients in Fig. 8. As can be seen from Fig. 8b, there are 7 cycles with a period of about 12 months in scale 18 and are 14 cycles with a period of about 6 months in scale 9. The higher coefficient in scale 18 (Fig. 8a) indicates that the groundwater level time series at well 30010 have a stronger annual variation characteristics apart from the feature of seasonal variation. Fig. 8c and d show that there are no permanent periods for InSAR time series at well 30010 from Jun. 2003 to Nov. 2013. As can be seen, there are 5.5 cycles with a lax period (because of the low coefficient in Fig. 8c) of about 15.6 months in scale 33. Nevertheless, the amplitudes show significant increase after 2011 in scale 33 and 59 in Fig. 8h.

#### 6.4. Relationship between land subsidence and urbanization

As reported by the China Geological Survey (CGS), land subsidence in Beijing was first recorded in 1950s, then spread rapidly throughout

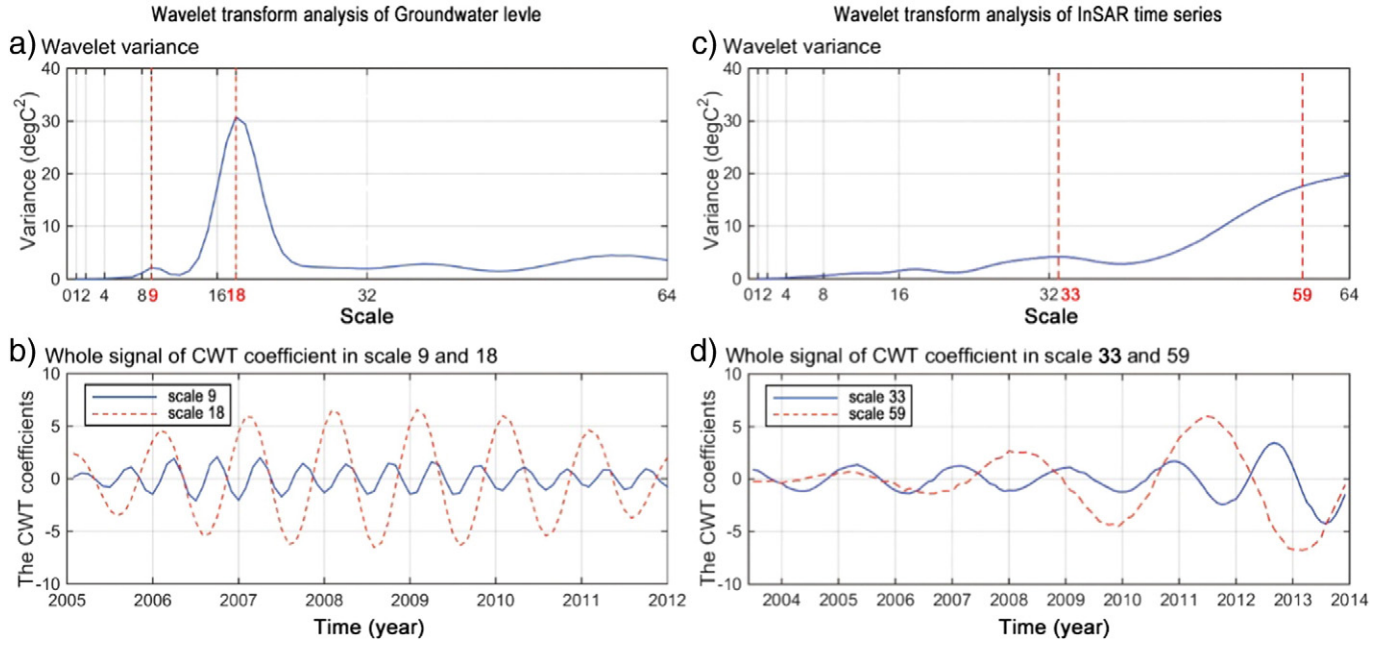


**Fig. 8.** (a) Wavelet variance curve of groundwater level time series at the location of well 30010. (b) The CWT coefficients curve of groundwater level time series in different scales. (c) and (d) are same as Fig. 8a and b but for InSAR time series.

the whole plain, with the rapid development of the industry and urbanization. Our group has analyzed the relationship between land subsidence and the urbanization (such as high buildings, high-density transportation network and high population) in Beijing. By creating an index-based built-up index (IBI) from Landsat TM image, we generated the time-varying static load field according to the period of the acquisitions used for InSAR measurements (Chen et al., 2015b). However, the study simply focused on the relationship between land subsidence and building density described by IBI despite other factors such as building structures, height and floor area ratio. The result showed that there was a positive correlation (The Spearman's rank correlation coefficient reached 0.312) between building density and land subsidence, especially for the areas with high density buildings or extensive transportation networks.

#### 6.5. Relationship between land subsidence and geological conditions

According to our previous works with regard to the land subsidence in Beijing, the distribution and development trend of the local land subsidence in eastern plain area are controlled by geological structures (Chen et al., 2016). There are several active high angle normal faults in the Beijing Plain as shown in Fig. 7a. As can be seen, the eastern subsidence zone (composed of southern Chaoyang and northern Tongzhou) is collectively controlled by the Liangxiang-qianmen-shuyi fault and Nanyuan-tongxian fault. The subsidence area in south Shunyi is mainly controlled by the Liangxiang-qianmen-shuyi fault, while the subsidence area in Changping is controlled by the Nankou-Sunhe fault and Huangzhuang-Gaoliying fault.

As mentioned in Section 2.1, Beijing Plain is a typical piedmont pluvial-alluvial plain composed of several alluvial-pluvial fans and an alluvial plain area. The aquifer on the top of the alluvial fans consists of cobbles and gravels; the middle part is full of sand gravel strata, while in the fringe part and alluvial plain area it gradually converted to the multi-layer structure of the coarse sand, medium sand, and fine sand. Nevertheless, previous studies show that the land subsidence in eastern Beijing Plain has connection with the quaternary compressible layers in spatial distribution (Yang et al., 2010; Zhou et al., 2016) e.g., the eastern subsidence bowl mostly lay the zone with a compressible deposits ranging from 150 to 180 m, while the subsidence area in southern Shunyi is

mostly situated in the zone with a compressible layers of around 90–120 m.

However, in local areas such as the airport, the distribution of subsidence is partly correlated to the groundwater table, but the causes of land subsidence are more complicated. In addition to natural processes as mentioned above, many anthropogenic processes such as surface loading (e.g., of buildings, planes, goods, and people), transportations (especially subway lines), impacts from airplane takeoff and landing, and underground facilities may jointly affect the ground displacement.

## 7. Conclusions

In this study, we have presented InSAR time-series analysis to investigate the long-term displacement of Capital International Airport in Beijing, China. An advanced InSAR time-series technique, referred to as SBAS, was performed on three SAR image stacks, and time-series measurements were obtained during the period of investigation from June 2003 to November 2013. The displacement rates have been estimated to have a maximum value of approximately –66.2 mm/year relative to the reference point. The projected mean vertical displacement rates are in good agreement with measurements estimated from ground leveling surveys: the correlation coefficient of the fitting result is 0.96, with a standard deviation of 1.9 mm/year and a mean difference of 2.0 mm/year.

From the time-series investigation, we detected two conspicuous subsidence bowls forming in the north of the airport area. One of these is located north of runway 36R, which has been sinking at a rate of less than –50 mm/year. Fortunately, the deformation of the subsid-ing runways is within the safe range according to the constructions standards.

Land subsidence in Beijing Plain is correlated with groundwater levels and is controlled by several active faults. Groundwater depth in Beijing Plain was increasing year by year despite the decrease of the groundwater exploitation. Then inelastic, permanent subsidence occurs where the aquifer system presents a continuous compaction associated with the groundwater level decrease. In this case, the land subsidence in this areas present an increasing trend in the rate, and is not consistent with the groundwater level. Other triggering factors, such as the quater-nary compressible layers and urbanization, also have different degrees

of contribution or impact on land subsidence. For local areas, the causes of land subsidence are more complicated, and we will continue our research on the mechanisms controlling subsidence in metropolitan areas.

## Acknowledgment

We thank the European Space Agency (ESA), for their great efforts in developing and distributing the remotely sensed SAR data and for their generosity in making parts of them available at no cost. We also thank the surveying and mapping departments in Beijing for the leveling and groundwater table data released to the public. This work was supported by the National Natural Science Foundation of China under Grant 41130744/D0107, 41171335/D010702, and D010702/4140010982. The provision of the Doris and StaMPS for data processing by TU Delft is gratefully acknowledged. The authors would like to thank Enago ([www.enago.cn](http://www.enago.cn)) for the English language review.

## Appendix A. Supplementary data

Supplementary data to this article can be found online at doi:10.1016/j.tecto.2016.10.016.

## References

- Aobpaet, A., Cuenca, M.C., Hooper, A., et al., 2013. InSAR time-series analysis of land subsidence in Bangkok, Thailand. *Int. J. Remote Sens.* 34 (8), 2969–2982.
- Berardino, P., Fornaro, G., Lanari, R., et al., 2002. A new algorithm for surface deformation monitoring based on small baseline differential SAR interferograms. *IEEE Trans. Geosci. Remote Sens.* 40 (11), 2375–2383.
- Calabro, M.D., Schmidt, D.A., Roering, J.J., 2010. An examination of seasonal deformation at the Portuguese Bend landslide, southern California, using radar interferometry. *J. Geophys. Res.* 115, F02020. <http://dx.doi.org/10.1029/2009JF001314>.
- Calderhead, A.I., Martel, A., Alasset, P.J., et al., 2010. Land subsidence induced by groundwater pumping, monitored by D-InSAR and field data in the Toluca Valley, Mexico. *Can. J. Remote. Sens.* 36 (1), 9–23.
- Chaussard, E., Wdowinski, S., Cabral-Cano, E., et al., 2014. Land subsidence in Central Mexico detected by ALOS InSAR time-series. *Remote Sens. Environ.* 140, 94–106.
- Chen, B., Gong, H., Li, X., et al., 2015a. Spatial-temporal evolution patterns of land subsidence with different situation of space utilization. *Nat. Hazards* 77 (3), 1–19.
- Chen, B., Gong, H., Li, X., et al., 2015b. Spatial correlation between land subsidence and urbanization in Beijing, China. *Nat. Hazards* 75 (3), 2637–2652.
- Chen, M., Tomás, R., Li, Z., et al., 2016. Imaging land subsidence induced by groundwater extraction in Beijing (China) using satellite radar interferometry. *Remote Sens.* 8 (6), 468–489.
- Dong, S., Samsonov, S., Yin, H., et al., 2014. Time-series analysis of subsidence associated with rapid urbanization in Shanghai, China measured with SBAS InSAR method. *Environ. Earth Sci.* 72 (3), 677–691.
- Feng, W., Li, Z., Hoey, T., et al., 2014. Patterns and mechanisms of coseismic and postseismic slips of the 2011 M<sub>W</sub> 7.1 Van (Turkey) earthquake revealed by multi-platform synthetic aperture radar interferometry. *Tectonophysics* 632, 188–198.
- Ferronato, M., Gambolati, G., Janna, C., et al., 2008. Numerical modelling of regional faults in land subsidence prediction above gas/oil reservoirs. *Int. J. Numer. Anal. Methods Geomech.* 32 (6), 633–657.
- Galloway, D., Jones, D.R., Ingebritsen, S.E., 1999. Land Subsidence in the US. U.S. Geological Survey Circular 1182. U.S. Geological Survey, Reston, Virginia, USA, p. 177. <http://pubs.usgs.gov/circ/circ1182/>.
- Gambolati, G., Ferronato, M., Teatini, P., et al., 2001. Finite element analysis of land subsidence above depleted reservoirs with pore pressure gradient and total stress formulations. *Int. J. Numer. Anal. Methods Geomech.* 25 (4), 307–327.
- Guo, L., Bo, W., Yang, G., 2003. Characteristics of current deformation of fault belts in north China. *Crustal Deform. Earthq.* 23 (2), 29–36 (in Chinese).
- Hanssen, R., 2001. *Radar Interferometry: Data Interpretation and Error Analysis*. Springer, New York.
- Higgins, S.A., Overeem, I., Steckler, M.S., et al., 2014. InSAR measurements of compaction and subsidence in the Ganges-Brahmaputra Delta, Bangladesh. *J. Geophys. Res. Earth Surf.* 119, 1768–1781. <http://dx.doi.org/10.1002/2014JF003117>.
- Hooper, A., 2008. A multi-temporal InSAR method incorporating both persistent scatterer and small baseline approaches. *Geophys. Res. Lett.* 35, L16302.
- Hooper, A., 2009. A Statistical-cost Approach to Unwrapping the Phase of InSAR Time Series. Proceeding of International Workshop on ERS SAR Interferometry, Frascati, Italy, 30 November–4 December 2009.
- Hooper, A., Bekkaert, D., Spaans, K., et al., 2012. Recent advances in SAR interferometry time series analysis for measuring crustal deformation. *Tectonophysics* 514, 1–13.
- Hooper, A., Bekkaert, D., Spaans, K., 2013. StaMPS/MTI (version 3.3b1), pp.22. [http://homepages.see.leeds.ac.uk/~earahoo/stamps/StaMPS\\_Manual\\_v3.3b1.pdf](http://homepages.see.leeds.ac.uk/~earahoo/stamps/StaMPS_Manual_v3.3b1.pdf).
- Hu, R.L., Yue, Z.Q., Wang, L.C., et al., 2004. Review on current status and challenging issues of land subsidence in China. *Eng. Geol.* 76 (1–2), 65–77.
- Hu, B., Wang, H.S., Sun, Y.L., et al., 2014. Long-term land subsidence monitoring of Beijing (China) using the small baseline subset (SBAS) technique. *Remote Sens.* 6 (5), 3648–3661.
- Jie, Y.X., Gao, Y., Li, G.X., 2007. Analysis on the land subsidence induced by city construction. *Geotech. Eng. Tech.* 21 (2), 78–82 (in Chinese).
- Krieger, G., Moreira, A., Fiedler, H., et al., 2007. TanDEM-X: a satellite formation for high-resolution SAR interferometry. *IEEE Trans. Geosci. Remote Sens.* 45 (11), 3317–3341.
- Lanari, R., Casu, F., Manzo, M., et al., 2007. An overview of the small BAseline subset algorithm: a DInSAR technique for surfacedeformation analysis. *Pure Appl. Geophys.* 164 (4), 637–661.
- Lazecký, M., Rapant, P., Perissin, D., et al., 2014. Deformations of highway over undermined Ostrava-Svinov area monitored by InSAR using limited set of SAR images. *Procedia Technol.* 16, 414–421.
- Liu, Y.Z., Wu, Q., Lin, P., et al., 2012a. Restudy of the storage and migration model of the quaternary groundwater in Beijing plain area. *Sci. China Earth Sci.* 55 (7), 1147–1158.
- Liu, M., Jia, S., Chu, H., 2012b. The monitoring system and technologies of land subsidence in Beijing. *Geol. Resour.* 21, 244–249 (in Chinese).
- Liu, D., Shao, Y., Liu, Z., et al., 2014. Evaluation of InSAR and TomoSAR for monitoring deformations caused by mining in a mountainous area with high resolution satellite-based SAR. *Remote Sens.* 6 (2), 1476–1495.
- Luo, Q., Perissin, D., Lin, H., et al., 2014. Subsidence monitoring of Tianjin suburbs by TerraSAR-X persistent scatterers interferometry. *IEEE J. Sel. Top. Appl. Earth Obs. Remote. Sens.* 7 (5), 1642–1650.
- Marie, M.M., Manoochehr, S., 2015. Spatiotemporal characterization of land subsidence and uplift in phoenix using InSAR time series and wavelet transforms. *J. Geophys. Res.* 120 (8), 5822–5842.
- Neelmeijer, J., Motagh, M., Wetzel, H., 2014. Estimating spatial and temporal variability in surface kinematics of the Inylchek Glacier, Central Asia, using TerraSAR-X data. *Remote Sens.* 6 (10), 9239–9259.
- Ng, A.H.M., Ge, L., Zhang, K., et al., 2012. Estimating horizontal and vertical movements due to underground mining using ALOS PALSAR. *Eng. Geol.* 143, 18–27.
- Perissin, D., Wang, Z., Lin, H., 2012. Shanghai subway tunnels and highways monitoring through Cosmo-SkyMed persistent scatterers. *ISPRS J. Photogramm. Remote Sens.* 73, 58–67.
- Raucoules, D., Maisons, C., Carnec, C., et al., 2003. Monitoring of slow ground deformation by ERS radar interferometry on the Vauvert salt mine (France): comparison with ground-based measurement. *Remote Sens. Environ.* 88 (4), 468–478.
- Ruch, J., Manconi, A., Zeni, G., et al., 2009. Stress transfer in the Lazufre volcanic area, central Andes. *Geophys. Res. Lett.* 36, L22303.
- Schmidt, D.A., Bürgmann, R., 2003. Time-dependent land uplift and subsidence in the Santa Clara valley, California, from a large interferometric synthetic aperture radar data set. *J. Geophys. Res.* 108 (B9), 2416–2428.
- Short, N., LeBlanc, A.M., Sladen, W., et al., 2014. RADARSAT-2 D-InSAR for ground displacement in permafrost terrain, validation from Iqaluit Airport, Baffin Island, Canada. *Remote Sens. Environ.* 141, 40–51.
- Shugar, D.H., Rabus, B.T., Clague, J.J., et al., 2012. The response of Black Rapids Glacier, Alaska, to the Denali earthquake rock avalanches. *J. Geophys. Res.* 117, F01006. <http://dx.doi.org/10.1029/2011JF002011>.
- Stramondo, S., Saroli, M., Tolomei, C., et al., 2007. Surface movements in Bologna (Po Plain—Italy) detected by multitemporal DinSAR. *Remote Sens. Environ.* 110 (3), 304–316.
- Stramondo, S., Bozzano, F., Marra, F., et al., 2008. Subsidence induced by urbanisation in the city of Rome detected by advanced InSAR technique and geotechnical investigations. *Remote Sens. Environ.* 112 (6), 3160–3172.
- Tizzani, P., Berardino, P., Casu, F., et al., 2007. Surface deformation of long valley caldera and mono basin, California, investigated with the SBAS-InSAR approach. *Remote Sens. Environ.* 108 (3), 277–289.
- Walter, T.R., Subandriyo, J., Kirbani, S., et al., 2015. Volcano-tectonic control of Merapi's lava dome splitting: the November 2013 fracture observed from high resolution TerraSAR-X data. *Tectonophysics* 639, 23–33.
- Wang, X., Liu, G., Yu, B., et al., 2014. 3D coseismic deformations and source parameters of the 2010 Yushu earthquake (China) inferred from DInSAR and multiple-aperture InSAR measurements. *Remote Sens. Environ.* 152, 174–189.
- Xie, J., Yang, G., Bo, W., 2002. Study on the regional deformation field and strong earthquake risk of Beijing area in the near future. *N. China Earthq. Sci.* 20 (1), 1–9 (in Chinese).
- Xue, Y., Zhang, Y., Ye, S., et al., 2005. Land subsidence in China. *Environ. Geol.* 48 (6), 713–720.
- Yang, Y., Jia, S., Wang, H., 2010. The status and development of land subsidence in Beijing plain. *Shanghai Geol.* 31 (4), 23–27 (in Chinese).
- Yang, C., Zhang, Q., Zhao, C., et al., 2014. Monitoring land subsidence and fault deformation using the small baseline subset InSAR technique: a case study in the Datong Basin, China. *J. Geodyn.* 75 (4), 34–40.
- Zhou, C., Gong, H., Chen, B., et al., 2016. Land subsidence under different land use in the eastern Beijing plain, China 2005–2013 revealed by InSAR time-series analysis. *GI Sci. Remote. Sens.* <http://dx.doi.org/10.1080/15481603.2016.1227297>.
- Zhu, L., Gong, H., Teatini, P., et al., 2015. Land subsidence due to groundwater withdrawal in the northern Beijing plain, China. *Eng. Geol.* 193, 243–255.